Journal of Computational Science 51 (2021) 101355

Contents lists available at ScienceDirect

Journal of Computational Science

journal homepage: www.elsevier.com/locate/jocs

Cubature rules for weakly and fully compressible off-lattice Boltzmann methods

Dominik Wilde [a,b,*], Andreas Krämer [c], Mario Bedrunka [b,a], Dirk Reith [b,d], Holger Foysi [a]

[a] Department of Mechanical Engineering, University of Siegen, Paul-Bonatz-Straße 9-11, 57076 Siegen-Weidenau, Germany
[b] Institute of Technology, Resource and Energy-efficient Engineering (TREE), Bonn-Rhein-Sieg University of Applied Sciences, Grantham-Allee 20, 53757 Sankt Augustin, Germany
[c] Department of Mathematics and Computer Science, Freie Universität Berlin, Arnimallee 6, 14195 Berlin, Germany
[d] Fraunhofer Institute for Algorithms and Scientific Computing (SCAI), Schloss Birlinghoven, 53754 Sankt Augustin, Germany

ARTICLE INFO

Keywords:
Lattice Boltzmann method
Cubature
Semi-Lagrangian
Gauss–Hermite quadrature
Compressible

ABSTRACT

Off-lattice Boltzmann methods increase the flexibility and applicability of lattice Boltzmann methods by decoupling the discretizations of time, space, and particle velocities. However, the velocity sets that are mostly used in off-lattice Boltzmann simulations were originally tailored to on-lattice Boltzmann methods. In this contribution, we show how the accuracy and efficiency of weakly and fully compressible semi-Lagrangian off-lattice Boltzmann simulations are increased by velocity sets derived from cubature rules, i.e., multivariate quadratures not produced by the Gauß-product rule. In particular, simulations of 2D shock-vortex interactions indicate that the cubature-derived degree-nine D2Q19 velocity set is capable of replacing the Gauß-product rule-derived D2Q25. Likewise, the degree-five velocity sets D3Q13 and D3Q21, as well as a degree-seven D3V27 velocity set were successfully tested for 3D Taylor–Green vortex flows to challenge and surpass the quality of the customary D3Q27 velocity set. In compressible 3D Taylor–Green vortex flows with Mach numbers $\mathrm{Ma} = \{0.5; 1.0; 1.5; 2.0\}$ on-lattice simulations with velocity sets D3Q103 and D3V107 showed only limited stability, while the off-lattice degree-nine D3Q45 velocity set accurately reproduced the kinetic energy provided by literature.

1. Introduction

The lattice Boltzmann method (LBM) [1–5] is an efficient approach for the numerical simulation of fluids. Compared to other methods discretizing the Boltzmann equation, such as discrete-velocity models [6,7] or (unified) gas-kinetic schemes [8,9], the LBM exhibits three key properties. First, the distribution functions are integrated along characteristics in time, leading to the well-known 0.5-shift in the relaxation time [10]. Second, the equilibrium distribution function is expressed as Hermite series, mostly of degree two, but higher for compressible [11] and thermal cases [12]. Third, the velocity space is integrated via quadrature rules, in particular by Gauß-Hermite quadratures [12,13]. By the latter, the unbounded velocity space of the Boltzmann equation is expressed by only a limited number of weighted particle velocities, tied together as a velocity set. The type of numerical integration with the underlying weight function $\exp\left(-|\mathbf{x}|^2\right)$ does not only appear in the LBM, but for instance also in Kalman filters [14]. Therefore, the literature on numerical integration is a good starting point for the search of well-suited velocity sets [15–17]. More specifically, the literature specifies two main approaches to derive the respective rules: Gauß-product rules and non-product rules [15]. The literature denotes multivariate non-product rules also as *cubature rules* [16,17].

The simpler and widely-used approach of the ones mentioned above is the Gauß-product rule, which is calculated by the outer product of a 1D quadrature. For example, the D1Q3 velocity set is essentially the 1D Gauß-Hermite quadrature constructed by the roots of the third-order Hermite polynomial [18]. By applying the Gauß-product rule, the D1Q3 is turned into a D2Q9 in two dimensions, and by applying the same rule once more, the D3Q27 velocity set is derived [18]. Since the number of particle velocities exceeds the number of the encoded physical moments, pruning the D3Q27 velocity set leads to the D3Q15 and D3Q19 sets with different high-order truncation errors [19–21]. A modification of the regular D3Q27 is the recently introduced crystallographic LBM [22], which expresses the particle distributions in a body-centered cubic arrangement of grid points. All above mentioned velocity sets fit into a regular grid, which is another key asset of the well-established on-lattice Boltzmann method, with the vector of the particle velocities ending on one of the neighboring

* Corresponding author at: Department of Mechanical Engineering, University of Siegen, Paul-Bonatz-Straße 9-11, 57076 Siegen-Weidenau, Germany.
E-mail address: wilde.aerospace@gmail.com (D. Wilde).

https://doi.org/10.1016/j.jocs.2021.101355
Received 21 December 2020; Received in revised form 2 March 2021; Accepted 19 March 2021
Available online 3 April 2021

grid points. For weakly compressible flows, this collection of velocity sets in combination with a second-order polynomial expansion of the Maxwell–Boltzmann equilibrium is widely used, although not perfect in terms of Galilean invariance, due to well-known errors in the stress tensor [23]. However, when a higher degree of precision for the numerical integration is needed [24,25], in particular for compressible [26] or dilute flows [27], the resulting velocity sets become unfeasible for two reasons. Firstly, Gauß-product rules suffer from the "curse of dimensionality", i.e., the number of abscissae rapidly increases, especially for high spatial dimensions with high degree of precision. Secondly, when derived from Hermite polynomials the degree-nine one-dimensional velocity set D1Q5 holds abscissae which do not fit on a regular grid, so that an even larger velocity set D1Q7 with equidistant abscissae must be used to obtain a sufficiently high integration order [28]. These multivariate lattices with equidistant nodes are constructed by solving the orthogonality relations [13,24,29].

Contrary to Gauß-product rules, the abscissae of cubature rules are not derived by quadratures of lower dimension. They are rather found individually for a certain pair of degree of precision and dimension. Due to this freedom of velocity discretization, off-lattice Boltzmann methods are required to apply them in the LBM. There is only a very limited number of publications, which display simulations using off-lattice velocity sets [30–32].

The present manuscript therefore derives velocity sets from cubature rules and explores them using the semi-Lagrangian lattice Boltzmann method (SLLBM, [33]), with applications to both weakly and fully compressible flows. In contrast to Eulerian time integration schemes like finite difference [34,35], finite volume [36,37], discontinuous Galerkin LBM schemes [38,39], the SLLBM inherits the Lagrangian time integration along characteristics from the LBM and recovers the off-lattice distribution function values by interpolation. Recent works [40–46] provided evidence that the SLLBM is a promising off-lattice Boltzmann method for the simulation of both weakly and fully compressible flows. However, these works used either on-lattice velocity sets, e.g. D2Q9, or D3Q27, or velocity sets that had been derived by the Gauß-product rule, e.g. D2Q25 from 1D Gauß-Hermite quadrature. This gap is closed by the present article. This work shows that cubature-based velocity sets significantly enhance off-lattice Boltzmann simulations in terms of both efficiency and accuracy.

The remainder of this manuscript is structured as follows. Quadrature and cubature in the LBM are briefly recapitulated in Section 2 with a list of all investigated velocity sets in this article. Section 3 details the semi-Lagrangian lattice Boltzmann model for both weakly and fully compressible flows. The results Section 4 studies three test cases: a compressible two-dimensional shock-vortex interaction and the three-dimensional Taylor–Green vortex both in the weakly and in the fully compressible regime, each of them requiring different equilibria and velocity sets. Sections 5 and 6 provide discussion and conclusion.

2. Cubature in lattice Boltzmann methods

Following [17], we consider the approximation of an integral of function $\mathcal{F}$

$$I(\mathcal{F}) = \int_{\Omega} \omega(\mathbf{x})\mathcal{F}(\mathbf{x})d\mathbf{x}, \tag{1}$$

with $\Omega \subseteq \mathbb{R}^D$, weight function $\omega(\mathbf{x}) \geq 0$ and dimensions $D \geq 2$ by quadrature or cubature rules of the form

$$C(\mathcal{F}) = \sum_{i=0}^{Q-1} w_i \mathcal{F}(\mathbf{x}_i), \tag{2}$$

with number of abscissae Q and discrete weights w_i.

The degree of a quadrature is defined as the largest integer d that yields $I(\mathcal{F}) = C(\mathcal{F})$ for all monomials of degree $\leq d$

$$\prod_{i=0}^{D-1} x_i^{j_i} \quad \text{with} \quad \sum_{i=0}^{D-1} j_i \leq d. \tag{3}$$

These cubature formulas are applied to the distribution function of the force-free BGK-Boltzmann equation

$$\frac{\partial f}{\partial t} + \boldsymbol{\xi} \cdot \nabla f = -\frac{1}{\lambda}\left(f - f^{\mathrm{eq}}\right), \tag{4}$$

with (unshifted) relaxation time λ, particle distribution function f, equilibrium distribution function f^{eq}, and particle velocities $\boldsymbol{\xi}$. To this end, the Hermite moments $\boldsymbol{a}^{(n)}$ are gained in the form [12,13]

$$\boldsymbol{a}^{(n)} = \int_{\mathbb{R}^D} f \boldsymbol{\mathcal{H}}^{(n)} d\boldsymbol{\xi}, \tag{5}$$

where $\boldsymbol{\mathcal{H}}^{(n)}$ is an nth-order Hermite polynomial. The distribution function f is expressed as a finite Hermite series

$$f \approx f^N = \omega(\boldsymbol{\xi}) \sum_{n=0}^{N} \frac{1}{n!} \boldsymbol{a}^{(n)} \boldsymbol{\mathcal{H}}^{(n)}, \tag{6}$$

with truncation order N [13] with the result that moments of order M are exactly represented, if $M \leq N$. The velocity space is discretized by replacing the integral of Eq. (5) by a weighted quadrature leading to

$$\boldsymbol{a}^{(n)} = \int_{\mathbb{R}^D} \omega(\boldsymbol{\xi}) \frac{f}{\omega(\boldsymbol{\xi})} \boldsymbol{\mathcal{H}}^{(n)} d\boldsymbol{\xi} \tag{7}$$

$$= \sum_{i=0}^{Q-1} \frac{w_i f(\boldsymbol{\xi}) \boldsymbol{\mathcal{H}}^{(n)}(\boldsymbol{\xi}_i)}{\omega(\boldsymbol{\xi}_i)} = \sum_{i=0}^{Q-1} f_i \boldsymbol{\mathcal{H}}_i^{(n)}, \tag{8}$$

with the replacements $f_i = w_i f(\boldsymbol{\xi})/\omega(\boldsymbol{\xi}_i)$ and $\boldsymbol{\mathcal{H}}^{(n)}(\boldsymbol{\xi}_i) = \boldsymbol{\mathcal{H}}_i^{(n)}$. From [47] it is known that moments of order M can be exactly determined by quadrature or cubature rules of degree $d \geq N + M$. In particular, for weakly compressible flows the order of the moments is usually limited to $N = 2$, although $N = 3$ cancels the cubic error when deriving the Navier–Stokes equations by a Chapman–Enskog analysis [13]. In contrast, fully compressible flows even require expansion order $N = 4$. By overcoming the restriction that abscissae $\boldsymbol{\xi}_i$ need to match a regular grid, cubature rules become applicable, provided they approximate the weight function

$$\omega(\boldsymbol{\xi}) = \frac{1}{(2\pi)^{D/2}} e^{-|\boldsymbol{\xi}|^2/2}. \tag{9}$$

In the literature, cubature rules are usually listed for the weight function $\tilde{\omega}(x) = \exp\left(-|\mathbf{x}|^2\right)$. To obtain a velocity set to approximate the moments in Eq. (7), the cubature's abscissae have to be scaled by $\sqrt{2}$. The lattice speed of sound c_s of these velocity sets is—unless otherwise specified—unity, $c_s = 1$, which also implies the reference temperature $T_0 = 1$.

The following velocity sets were identified to be subject of an in-depth examination:

- First, the newly introduced degree-nine D2Q19 was compared to the D2Q25 derived from Gauß-product rule for fully compressible two-dimensional flows. The shape of D2Q19 is shown in Fig. 1
- Second, D3Q13 and D3Q21 velocity sets were applied to weakly compressible flows. The D3Q13 based on an icosahedron was already used in a weakly compressible finite difference LBM with a triangular mesh [32], whereas the D3Q21 derived from a dodecahedron has not been examined so far. Both platonic solids, shown in Fig. 2, possess a high geometric isotropy, i.e. the flow information encoded into the distribution function values is transported by regularly spaced abscissae ending on the surface of a sphere. The weights and abscissae of the D3Q13 and D3Q21 velocity sets are listed in Tables 2 and 3, respectively. Both velocity sets were compared to the customary D3Q27 on-lattice velocity set and in addition to a degree-seven velocity set, which we call D3V27 [15]. This velocity set is not affected by the cubic error in the stress tensor that troubles degree-five velocity sets. Although in the same spirit, it is not identical to the velocity set presented by Yudistiawan et al. [31].

Table 1
Quadrature and cubature rules utilized in the present article. Notation $E^{Q}_{D,n}$ according to Stroud [15] with number of abscissae Q, dimension D, and degree of precision d.

Name	$E^{Q}_{D,d}$	Remarks	Sources
D2Q19	$E^{19}_{2,9}$	Cubature rule by Haegemans and Piessens	[48], Appendix C
D2Q25	$E^{25}_{2,9}$	Gauß-product rule from 1D degree-nine Gauß-Hermite quadrature	[28]
D3Q13	$E^{13}_{3,5}$	Derived by the vertices of an icosahedron	[15,32], Table 2
D3Q21	$E^{21}_{3,5}$	Derived by the vertices of a dodecahedron	[15], Table 3
D3Q27	$E^{27}_{3,5}$	Doubly applied Gauß-product rule from 1D Gauß-Hermite quadrature	[49]
D3V27	$E^{27}_{3,7}$	Cubature rule by Stroud and Secrest.	[15]
D3Q45	$E^{45}_{3,9}$	Cubature rule by Konyaev.	[50,51], Appendix E
D3Q103	$E^{103}_{3,9}$	On-lattice velocity set	[25]
D3V107	$E^{107}_{3,9}$	On-lattice velocity set	[30]

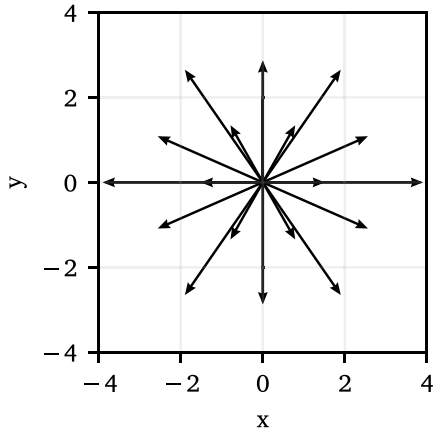

Fig. 1. Shape of the D2Q19 velocity set.

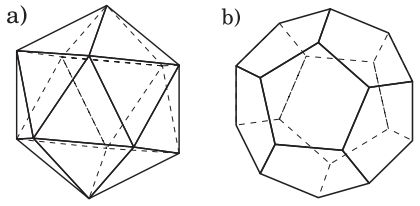

Fig. 2. Shape of icosahedron (a) and dodecahedron (b), which are the bases for the velocity sets D3Q13 and D3Q21 used in this work.

- Last, for three-dimensional compressible flows, a recently introduced D3Q45 velocity set was applied [52], based on a cubature rule by Konyaev [50,51]. This off-lattice velocity set was compared in an off-lattice Boltzmann simulation to the state of the art on-lattice counterparts D3Q103 and D3V107 applied to compressible on-lattice Boltzmann simulations.

Table 1 designates the velocity sets, which were used for the simulations in this article. The additional notation $E^{Q}_{D,d}$ follows the literature on multivariate quadratures integrating the weight function $\tilde{\omega}(x) = \exp\left(-|\mathbf{x}|^2\right)$, listing dimension D, degree d and number of abscissae Q. To identify the suitability of the introduced velocity sets beforehand, the symmetry conditions in Appendix B were successfully tested [53]. For example, a degree-five velocity set only reproduces the symmetry condition up to fifth order, whereas degree-nine velocity sets will also correctly reproduce the symmetry conditions up to ninth order.

3. Model description

The lattice Boltzmann equation reads

$$f_i(\mathbf{x}+\boldsymbol{\xi}_i\delta_t, t+\delta_t) = f_i(\mathbf{x},t) - \frac{1}{\tau}\left(f_i(\mathbf{x},t) - f_i^{\mathrm{eq}}(\mathbf{x},t)\right) \tag{10}$$

Table 2
Abscissae ξ_i and weights w_i for the D3Q13 velocity set, based on an icosahedron [4,15,32] with $r^2 = (5+\sqrt{5})/2$ and $s^2 = (5-\sqrt{5})/2$. The lattice speed of sound is $c_s = 1$.

i	w_i	ξ_i
0	2/5	$(0,0,0)$
$1,\dots,4$	1/20	$(0,\pm r,\pm s)$
$5,\dots,8$	1/20	$(\pm s,0,\pm r)$
$9,\dots,12$	1/20	$(\pm r,\pm s,0)$

Table 3
Abscissae ξ_i and weights w_i for the D3Q21 velocity set, based on a dodecahedron [15] with $\phi = (1+\sqrt{5})/2$. The lattice speed of sound c_s is $c_s = \sqrt{3/5}$.

i	w_i	ξ_i
0	2/5	$(0,0,0)$
$1,\dots,8$	3/100	$(\pm1,\pm1,\pm1)$
$9,\dots,12$	3/100	$(0,\pm\phi,\pm1/\phi)$
$13,\dots,16$	3/100	$(\pm1/\phi,0,\pm\phi)$
$17,\dots,20$	3/100	$(\pm\phi,\pm1/\phi,0)$

with relaxation time $\tau = \nu/(c_s^2\delta_t)+0.5$ depending on kinematic viscosity ν, and time step size δ_t.

This work applies the discrete equilibrium distribution function based on an expansion in terms of Hermite polynomials

$$f_i^{\mathrm{eq},N}(\mathbf{x},t) = w_i \sum_{n=0}^{N} \frac{1}{n!}\boldsymbol{a}_{eq}^{(n)}(\mathbf{x},t) : \boldsymbol{\mathcal{H}}_i^{(n)}, \tag{11}$$

with ":" denoting full contraction, w_i the discrete weights and N the expansion order. Both the moments $\boldsymbol{a}_{eq}^{(n)}$ and the Hermite tensors $\boldsymbol{\mathcal{H}}_i^{(n)}$ are listed in Appendix. In the weakly compressible case the local temperature $\theta = T/T_0$ is set to $\theta = 1$ with vanishing terms for second and higher order moments. Using Eq. (7) the moments density and momentum are obtained

$$\rho = \sum_{i=0}^{Q-1} f_i \tag{12}$$

$$\rho\mathbf{u} = \sum_{i=0}^{Q-1} \boldsymbol{\xi}_i f_i. \tag{13}$$

Compared to the standard LBM, the SLLBM replaces the node-to-node streaming step by a cell-wise interpolation procedure using interpolation polynomials ψ of interpolation order p to obtain the departure points, whose locations are dictated by the respective reversed particle velocities $f_i(\mathbf{x}-\delta_t\boldsymbol{\xi}_i)$, i.e. for all $\mathcal{M}$ points $\mathbf{x}$ in each cell Ξ:

$$f_i(\mathbf{x},t) = \sum_{j=1}^{\mathcal{M}} \hat{f}_{i\Xi j}(t)\psi_{\Xi j}(\mathbf{x}), \tag{14}$$

with $\hat{f}_{i\Xi j}$ denoting the distribution function value at the support points in each cell.

Gauß-Lobatto-Chebyshev points were used for the distribution of support points in the cells [33,44].

For the compressible test cases in Sections 4.1 and 4.3 we employed the recently introduced compressible SLLBM [44] with the following extensions. A second distribution function g is introduced to enable the calculation of flows with variable heat capacity ratio γ [47], following the same collide-and-stream algorithm as applied to the distribution function f.

$$g_i(\mathbf{x}+\boldsymbol{\xi}_i\delta_t, t+\delta_t) = g_i(\mathbf{x},t) - \frac{1}{\tau}\left(g_i(\mathbf{x},t) - g_i^{\mathrm{eq}}(\mathbf{x},t)\right) \tag{15}$$

The equilibrium of g is determined by the relation

$$g_i^{\mathrm{eq}} = \theta(2C_v - D)f_i^{\mathrm{eq}}, \tag{16}$$

with heat capacity at constant volume C_v. To complement Eqs. (12) and (13), the local temperature θ is determined by

$$2\rho C_v\theta = \sum_{i=0}^{Q-1}\left(|\zeta_i|^2\frac{f_i}{T_0} + g_i\right), \tag{17}$$

with peculiar particle velocity $\boldsymbol{\zeta}_i = \boldsymbol{\xi}_i - \mathbf{u}$.

The local speed of sound c_s^* consequently depends on the local relative temperature θ and on the heat capacity ratio γ, via

$$c_s^* = c_s\sqrt{\theta\gamma}. \tag{18}$$

The relaxation time τ in the compressible case is dependent on the local pressure P, i.e. $\tau = \mu/(c_s^2\delta_t P) + 0.5$ with dynamic viscosity μ. In addition, a quasi-equilibrium approach was used to vary the Prandtl number Pr. More details about the compressible SLLBM solver are listed in [44]. The NATriuM solver was used for the off-lattice Boltzmann simulations [45], which is based on the finite element library deal.ii [54]. The on-lattice Boltzmann simulations were performed using the lettuce software [55,56], being based on the GPU-accelerated machine learning toolkit PyTorch [57].

4. Results

The present work considers three test cases to evaluate the introduced velocity sets: the two-dimensional shock-vortex interaction, comparing the degree-nine velocity sets D2Q19 and D2Q25. This flow challenges the solver by acoustic emissions by the vortex downstream the shock. Next, the weakly compressible three-dimensional Taylor–Green vortex [58] was simulated by various 3D velocity sets, e.g. D3Q13, D3Q21, D3V27 and D3Q27 to explore the capability of the velocity sets to deal with underresolved flows. Finally, simulations of fully compressible 3D Taylor–Green vortex flows were explored with Mach numbers 0.5, 1.0, 1.5, and 2.0. This test case exhibits shocklets and viscous effects and features a standardized initialization. The on-lattice simulations were performed using the D3Q103 and D3V107 velocity sets, while the off-lattice simulations were run by the D3Q45 velocity set.

4.1. Compressible 2D shock vortex interaction

The compressible two-dimensional shock-vortex interaction was tested as a first test case to compare the two velocity sets D2Q19 and D2Q25. This benchmark was intensively studied by Inoue and Hattori [59], with the following setup. Two regions with $\mathrm{Ma}_a = 1.2$ and Ma_b determined by Rankine–Hugoniot conditions are divided by a steady shock. The Reynolds number is defined as $\mathrm{Re} = c_{s,\infty}^* R/\nu_\infty$ with subscript ∞ denoting the inflow conditions. The flow field of the vortex is given by

$$u_\theta(r) = \sqrt{\gamma T}\mathrm{Ma}_\mathrm{v}\, r\exp((1-r^2)/2), \tag{19}$$

where Ma_v denotes the Mach number of the vortex. The initial pressure and density field are

$$P(r) = \frac{1}{\gamma}\left(1 - \frac{\gamma-1}{2}\mathrm{Ma}_\mathrm{v}\exp(1-r^2)\right)^{\gamma/(\gamma-1)} \tag{20}$$

Table 4
Simulation setup of the compressible 2D shock vortex interaction.

Test case		(a)	(b)
Reynolds number	Re	400	800
Vortex Mach number	Ma_v	0.5	0.25
Advection Mach number	Ma_a	1.2	1.2
Relaxation time at $\theta = 1.0$	τ	3.82	2.16
Minimal spatial resolution	δ_x	0.003	0.003
Temporal resolution	δ_t	0.002	0.002
Interpolation polynomial order	p	4	4
Truncation order of equilibrium	N	4	4

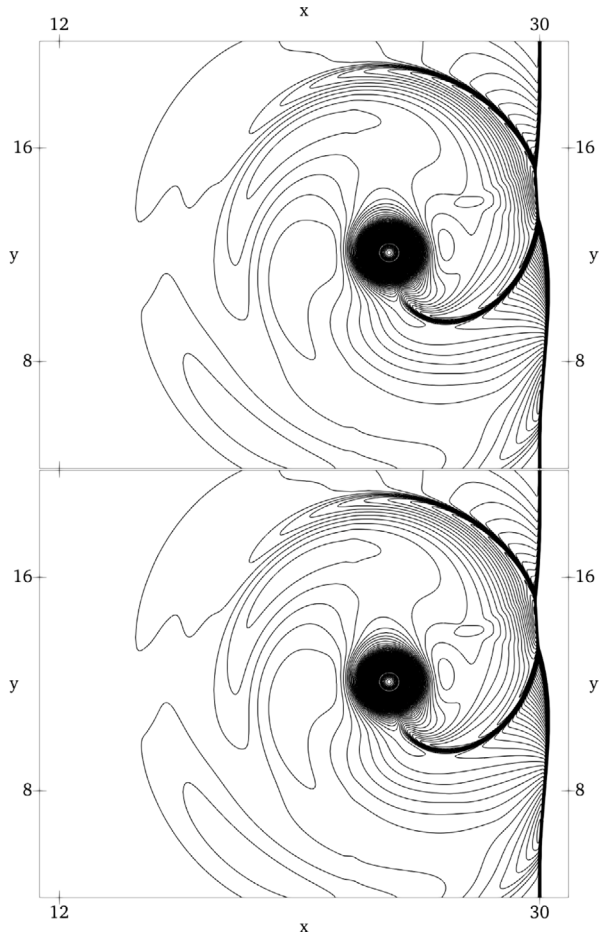

Fig. 3. Density contours of the shock-vortex interaction with $Ma_v = 0.5$ and $Re = 400$ in the range $\rho \in [0.92, 1.55]$ in 119 steps with velocity sets D2Q19 (top) and D2Q25 (below). No significant difference is visible despite the D2Q19's 24 percent reduction in computational cost.

and

$$\rho(r) = \left(1 - \frac{\gamma-1}{2}\mathrm{Ma}_\mathrm{v}\exp(1-r^2)\right)^{1/(\gamma-1)}. \tag{21}$$

The resolution was 256×256 cells with polynomial order $p = 4$, i.e., 1024×1024 grid points for the physical domain of $60R \times 24R$. Initially the center of the vortex was located at $x_\mathrm{v} = 32$, while the shock was located at $x_\mathrm{shock} = 30$. Likewise as in [44] we used a stretched grid to spatially resolve the shock region. The time step size was $\delta_t = 0.002$ with characteristic time $t' = R/c_{s,\infty}^*$. The Prandtl number was $\mathrm{Pr} = 0.75$ in all cases. Table 4 designates the most important parameters of the simulations. Fig. 3 depicts the density contours at $t = 8$ for test case (a) with $\mathrm{Ma}_\mathrm{v} = 0.5$, $\mathrm{Re} = 400$ and provides evidence that there is no significant difference between the simulations run by the D2Q19 and D2Q25 velocity sets.

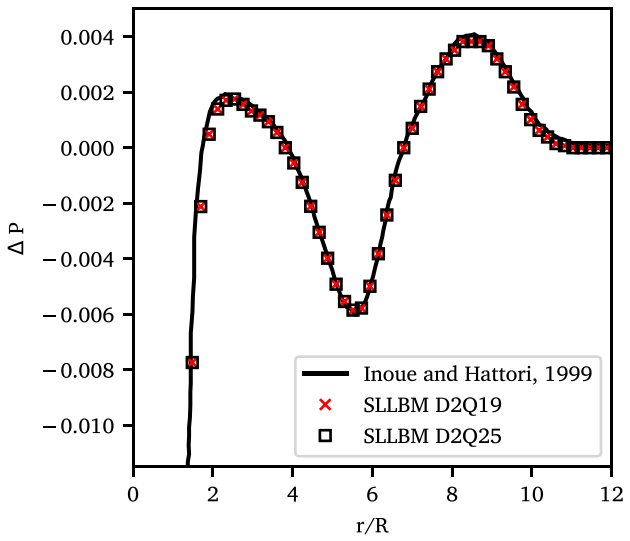

Fig. 4. Comparison of D2Q19 and D2Q25 in terms of the sound pressure $\Delta P = (P - P_B)/P_B$ of the shock-vortex interaction with $Re = 800, Ma_v = 0.25$ and at time $t' = 8'$ measured from the center of the vortex along the radius with 135° with respect to the x-axis. The SLLBM match the reference by Inoue and Hattori [59] well.

The evaluation of the sound pressure for test case (b) at $\mathrm{Ma}_v = 0.25$ and $\mathrm{Re} = 800$ confirms this observation, see in Fig. 4. The sound pressure $\Delta P = (P - P_B)/P_B$, with subscript B denoting the pressure downstream, was measured at time $t = 8$ from the center of the vortex along the 135° inclined radius with respect to the x-axis. As expected, the sound pressure of both SLLBM simulations matched the reference solution by Inoue and Hattori [59]. These findings approve the cubature-derived D2Q19 as a potent alternative for compressible off-lattice simulations to the D2Q25 being based on the Gauß-product rule used in previous works [41,44].

4.2. Weakly compressible 3D incompressible Taylor–Green vortex

The three-dimensional Taylor Green vortex served as a test case to apply the degree-five velocity sets D3Q13, D3Q21, and degree-seven D3V27 in comparison to the customary degree-five D3Q27 using an isothermal configuration $\theta = 1$ with truncation order of the equilibrium $N = 2$ for D3Q13, D3Q21, and D3Q27. By contrast, the D3V27 simulation exhibits a higher truncation order $N = 3$. The Mach number was $\mathrm{Ma} = 0.1$. The computational domain was $S = [0, 2\pi]^3$ and the following initial conditions were used

$$\boldsymbol{u}(\boldsymbol{x}, t = 0) = \begin{pmatrix} \sin(x)\cos(y)\cos(z) \\ -\cos(x)\sin(y)\cos(z) \\ 0 \end{pmatrix}, \tag{22}$$

$$P(\boldsymbol{x}, t = 0) = \frac{1}{16}(\cos(2x) + \cos(2y))\cos(2z + 2), \tag{23}$$

The kinetic energy of the flow is defined as

$$k = \frac{1}{(2\pi)^3} \int_S \frac{1}{2}|\mathbf{u}|^2 \, d^3\mathbf{x} \tag{24}$$

and the enstrophy as a measure of the dissipation with respect to the resolved scales [60]

$$\mathcal{E} = \frac{1}{(2\pi)^3} \int_S (\nabla \times \mathbf{u})^2 \, d^3\mathbf{x}. \tag{25}$$

As explained in detail in [33] and references therein, the scaled enstrophy $\nu\mathcal{E}$ measures the physical dissipation in terms of the local shear stresses. In turn, its deviation from the phenomenological dissipation rate $-dk/dt$ provides a measure for the numerical dissipation due to discretization.

Table 5
Simulation setup of the weakly compressible 3D Taylor–Green vortex.

Test case		(a)	(b)
Reynolds number	Re	400	1600
Mach number	Ma	0.1	0.1
Relaxation time	τ	0.517	0.508
Spatial resolution	δ_x	0.05	0.05
Temporal resolution	δ_t	0.0015	0.00075
Interpolation polynomial order	p	4	4
Truncation order of equilibrium	N	2[a]	2[a]

[a] $N = 3$ for D3V27.

Table 6
Root mean squared error of the scaled enstrophy with respect to the Ref. [58].

	D3Q13	D3Q21	D3V27	D3Q27
$\|\nu\mathcal{E}^{\mathrm{ref}} - \nu\mathcal{E}^{\mathrm{sim}}\|$	0.00141	0.00116	0.00107	0.00158

First, a well-resolved flow was tested by setting the Reynolds number to $Re = 400$. The domain was discretized by 32^3 cells with order of finite element $p = 4$, resulting in 128^3 grid points. The velocity sets were scaled in such a way that the time step size was $\delta t = 0.0015$ in all cases. A summary of the flow variables is listed in Table 5.

Fig. 5 depicts the dissipation dk/dt and the scaled enstrophy $\nu\mathcal{E}$ of the four focused velocity sets in comparison to the reference by Brachet et al. [58]. It is shown that all velocity sets match the reference solution for both dissipation and scaled enstrophy. Thus in the case of well-resolved simulations, even the lean D3Q13 velocity set commended itself as a good choice for three-dimensional flow simulations. In the case of the underresolved simulations with Reynolds number $\mathrm{Re} = 1600$ with time step size $\delta_t = 0.00075$, the situation is slightly different though, displayed in Fig. 6 showing different evolutions of dissipation and scaled enstrophy for each of the velocity sets. Initially, the dissipation followed the DNS reference simulation. As the flow entered the fully turbulent regime, the dissipation became more volatile than in the resolved case due to the under-resolution of small vortices. In this phase, the numerical discretization provided dissipation in the spirit of an implicit LES [61]. Despite the absence of an explicit subgrid model, all stencils produced macroscopic dissipation rates that roughly followed the reference solution. The D3Q13 and D3Q27 stencils even captured the location of the dissipation peak within 0.5 time units, whereas D3Q21 and D3V27 produced a plateau and a premature peak, respectively. That said, the broader implications of this difference are debatable since the dissipation in the under-resolved regime is mostly a result of numerical errors interacting with the finest resolved scales. In contrast, the scaled enstrophy is a more meaningful observable as it directly reflects the local shear stresses. Fig. 7 compares the scaled enstrophies revealing that the enstrophy determined by simulations with the common D3Q27 most drastically underestimated the enstrophy in this configuration. Table 6 confirms this observation by listing the Euclidean norm of the difference between the scaled enstrophies obtained by simulation and reference, i.e.

$$\|\nu\mathcal{E}^{\mathrm{ref}} - \nu\mathcal{E}^{\mathrm{sim}}\| = \sqrt{\frac{1}{\hat{N}} \sum_{j=1}^{\hat{N}} \left(\nu\mathcal{E}_j^{\mathrm{ref}} - \nu\mathcal{E}_j^{\mathrm{sim}}\right)^2}, \tag{26}$$

where $\hat{N}$ is the number of discrete measurements. The degree-seven D3V27 simulations as well as the degree-five D3Q21 simulations both more accurately predicted the scaled enstrophy.

4.3. Compressible 3D Taylor–Green vortex

As a final test case the compressible 3D Taylor–Green vortex was simulated. Recently, this test case has been by extensively investigated by Peng and Yang [62]. The Reynolds number was $Re = 400$, the heat

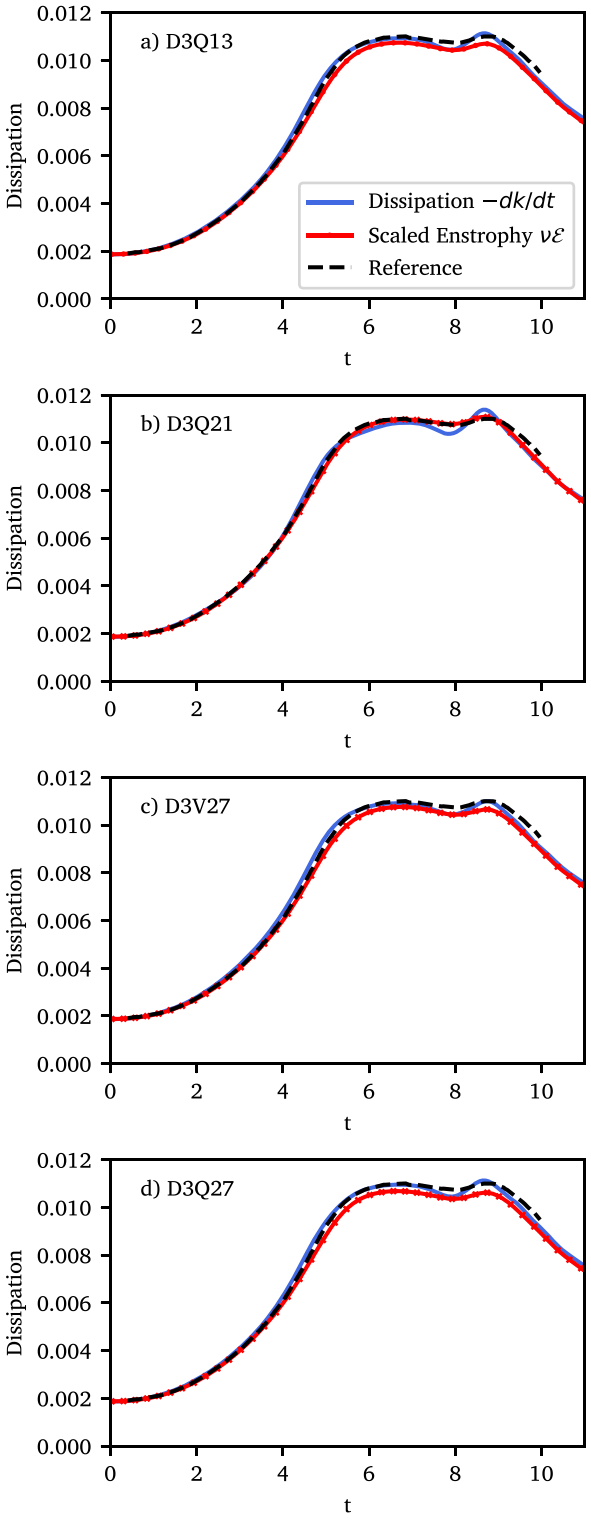

Fig. 5. Dissipation and scaled enstrophy over time from simulations of the three-dimensional Taylor–Green vortex at Reynolds number Re = 400 using the velocity sets D3Q13 (a), D3Q21 (b), D3V27 (c), and D3Q27 (d). For this well-resolved simulation at $N = 128^3$ both the dissipation $-dk/dt$ and the scaled enstrophy $\nu\mathcal{E}$ matched the reference solution well for all velocity sets considered.

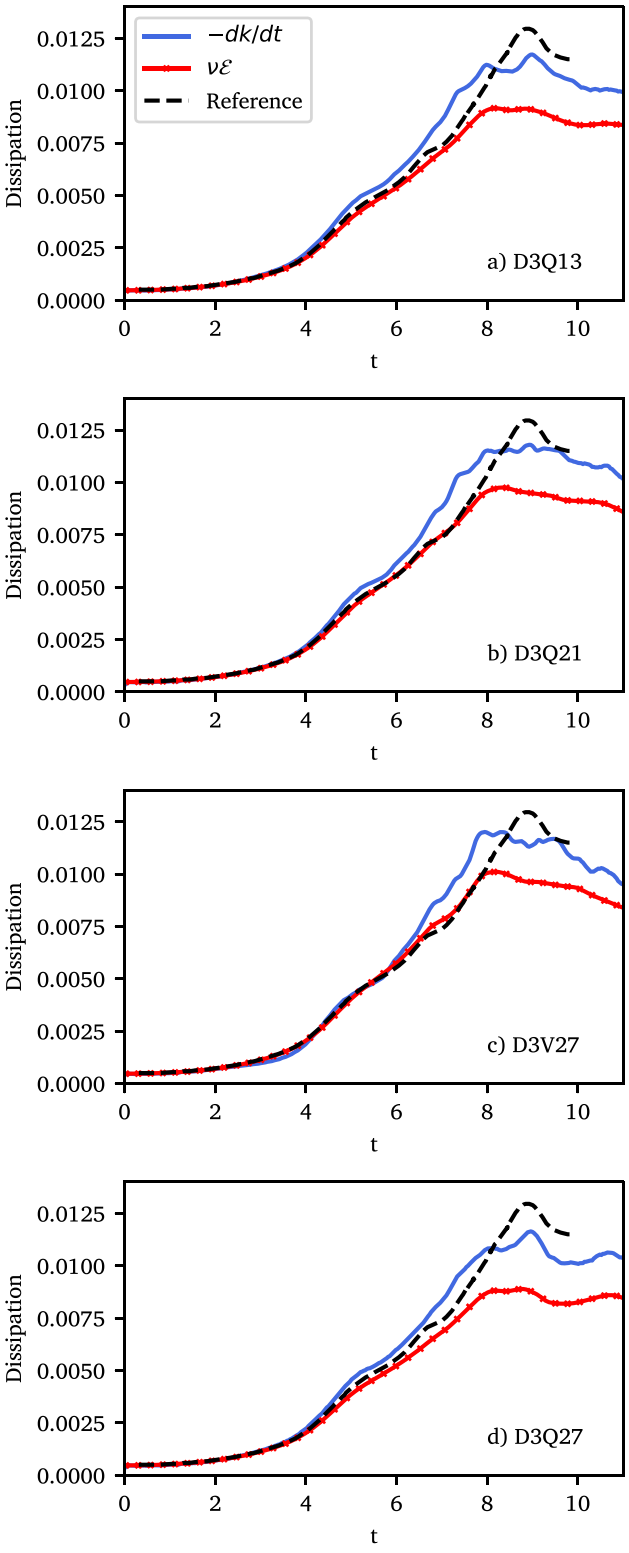

Fig. 6. Dissipation $-kE/dt$ and scaled enstrophy over time from simulations of the three-dimensional Taylor–Green vortex at Reynolds number Re = 1600 using the velocity sets D3Q13 (a), D3Q21 (b), D3V27 (c), and D3Q27 (d). This under-resolved simulation at $N = 128^3$ reveals differences for the dissipation and scaled enstrophy for the respective velocity sets.

capacity ratio was $\gamma = 1.4$, and the Prandtl number was Pr = 0.75. The initial velocity field corresponds to Eq. (22), whereas the pressure is obtained by $P = \rho T_0$ with $T_0 = 1$, and density

$$\rho(\boldsymbol{x}, t = 0) = 1.0 + \frac{C^2}{16}(\cos(2x) + \cos(2y))\cos(2z + 2). \tag{27}$$

This relation of temperature and density corresponds to the constant temperature initial condition (CTIC) detailed in Peng and Yang [62]. The numerator C can be either set to $C = \mathrm{Ma}^2$ or to $C = 1$; this work

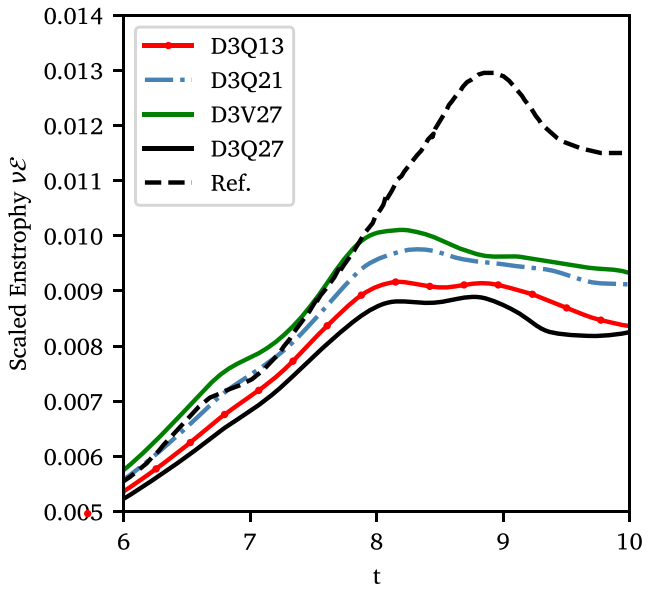

Fig. 7. Comparison of the scaled enstrophies $\nu\mathcal{E}$ shown in Fig. 6.

Table 7
Simulation setup of the fully compressible 3D Taylor–Green vortex.

Test case		(a)	(b)	(c)	(d)
Reynolds number	Re	400	400	400	400
Mach number	Ma	0.5	1.0	1.5	2.0
Spatial resolution	δ_x	0.025	0.025	0.025	0.025
Truncation order of equilibrium	N	4	4	4	4

made use of the latter. Table 7 lists the most important simulation variables and Table 8 separately lists the time step sizes and relaxation times at $\theta = 1.0$ of the respective simulations with the velocity sets D3Q103, D3V107, and D3Q45. The time step sizes of the on-lattice velocity sets were dictated by the configuration, whereas the time step sizes of the D3Q45 SLLBM simulation were adjustable. The results of the D3Q45 velocity set is discussed in more depth in a follow-up manuscript [52].

Fig. 8 depicts the mean kinetic energy over time for a resolution of 256^3 obtained by the velocity sets D3Q103, D3V107 and by the SLLBM D3Q45 simulation. It displays that the reference by Peng and Yang was well captured for Mach numbers Ma = 0.5 and Ma = 1.0 by all three velocity sets. However, the on-lattice simulations became unstable for the larger Mach numbers Ma = 1.5 and Ma = 2.0.

These results confirm the assumptions of other works which predicted the capability of the on-lattice velocity sets D3Q103 and D3V107 to simulate compressible flows [25,29,30,63]. However, simulations applying these velocity sets lack stability, at least in the present configuration for Mach numbers exceeding one. In contrast, the variable time step size of the SLLBM enabled stable simulations even at higher Mach numbers using a substantially smaller velocity set with 45 discrete velocities.

5. Discussion

The discretization of the velocity space by quadrature is a key asset of the lattice Boltzmann method. However, the coupling of the velocity space discretization with the spatial and temporal discretization in on-lattice Boltzmann methods is obstructive to find sufficiently small velocity sets especially for high quadrature order. Even a recent systematic study as done by Spiller and Dünweg did not yield smaller velocity sets than the already known D3Q103 [64], whose number of abscissae therefore appears to be the lower limit at this quadrature

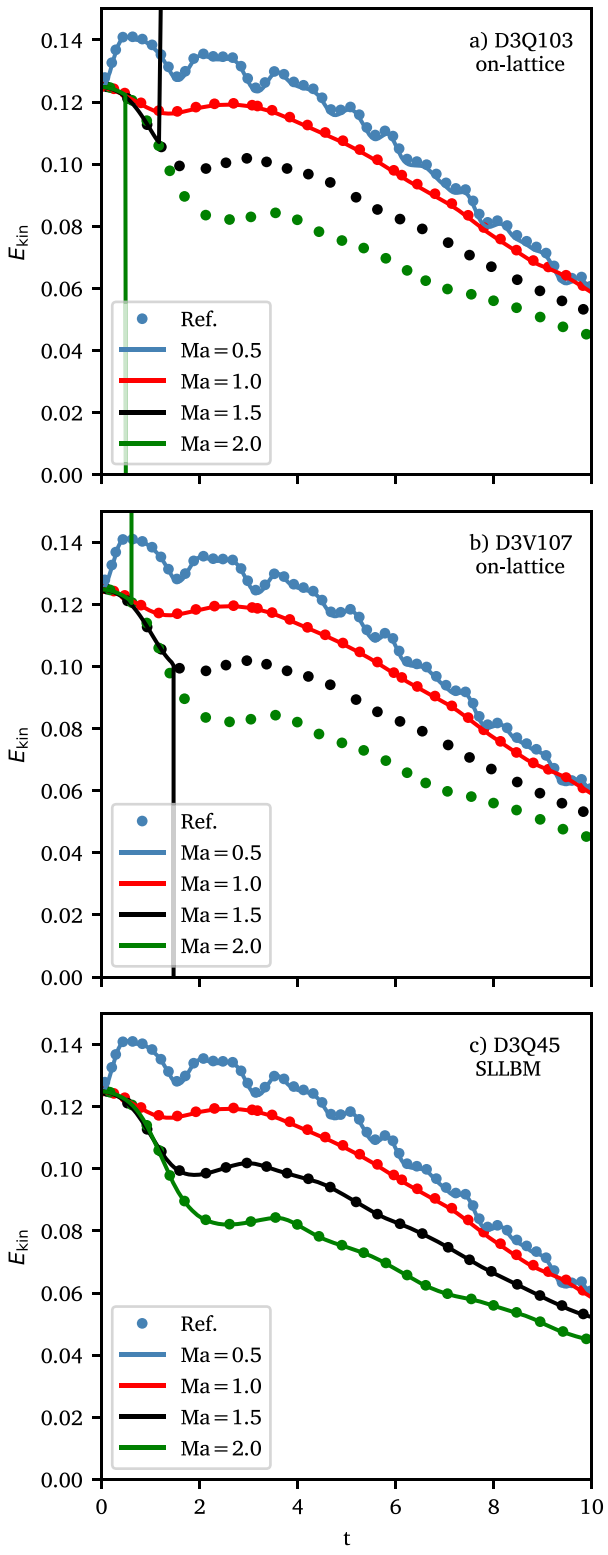

Fig. 8. On-lattice simulations utilizing the D3Q103 (a) and the D3V107 (b) in comparison to the SLLBM D3Q45 simulation (c). All velocity sets accurately reproduced the kinetic energies for the medium Mach numbers Ma = 0.5 and Ma = 1.0, while the on-lattice simulations failed for the higher Mach numbers Ma = 1.5 and Ma = 2.0. By contrast, the flexible time step size enabled successful SLLBM simulations even at the highest Mach numbers.

degree with equidistant nodes. The enormous size of these high-degree sets prevented their application in actual simulations, at least up to

Table 8
Time step sizes (top) and relaxation times at $\theta = 1.0$ (bottom) of the compressible Taylor–Green vortex simulations.

(a) Time step size δ_t	D3Q103	D3V107	D3Q45
Ma = 0.5	0.0121	0.0136	0.0165
Ma = 1.0	0.0243	0.0271	0.0329
Ma = 1.5	0.0364[a]	0.0407[a]	0.0178
Ma = 2.0	0.0485[a]	0.0542[a]	0.0119
(b) Relaxation time τ	D3Q103	D3V107	D3Q45
Ma = 0.5	0.572	0.564	0.553
Ma = 1.0	0.644	0.629	0.606
Ma = 1.5	0.716[a]	0.694[a]	0.943
Ma = 2.0	0.789[a]	0.758[a]	1.681

[a]Unstable simulations.

the present study. The simulations of the fully compressible Taylor–Green vortex in the present work show that on-lattice velocity sets are generally feasible for compressible simulations, but they lack stability at Mach numbers beyond unity. The biggest issue, from our point of view, is the fixed time step size of most compressible on-lattice Boltzmann methods. An exception to this are hybrid lattice Boltzmann methods, which solve the energy equation by finite volume or finite difference methods [65–67]. These methods are capable of adjusting the time step size by changing the reference temperature, but they suffer from restrictions in the stability regions [68]. Despite the successes of recent works [26,42,69–71], the applicability of compressible on-lattice Boltzmann methods remains vague. Although shifted stencils have proven to extend the Mach number range of on-lattice Boltzmann methods [72,73] in certain situations, the Taylor–Green vortex at high Mach numbers would still not be stable with static reference frames. Solely dynamic shifts of the reference frame as presented by Coreixas and Latt [74] might be an alternative for on-lattice Boltzmann methods, although they cause additional computational costs and require further investigation.

Compared to on-lattice Boltzmann methods, the discretization of the velocity space is a largely unexplored field of research in off-lattice Boltzmann methods. We were able, however, to identify a large potential in equipping off-lattice Boltzmann methods with velocity sets with significantly different shapes. Instead of deriving stencils case-by-case, the research on multivariate quadrature rules yielded suitable cubature rules as templates for velocity sets. Consequently, this work's main purpose was to explore these velocity sets by off-lattice Boltzmann simulations.

The results in Section 4 clearly indicate that the spatial freedom obtained in the collocation of abscissae, as done in cubature rules, reduces the number of discrete velocities significantly. Simultaneously, the computational costs halved, narrowing the gap between on-lattice and off-lattice Boltzmann methods in terms of efficiency. For example, the D2Q19 degree-nine velocity set is approximately half the size of its on-lattice counterpart D2V37 with equal quadrature order [24]. The difference between the D3Q45 and the D3Q103 velocity set is even more significant, but the size of the D3Q45 is also superior compared to a recently utilized degree-nine D3Q77 off-lattice velocity set for compressible finite volume LBMs [75]. The D3Q45 simulations of the Taylor–Green vortex proved to be stable and accurate even for high Mach number flows. This can be attributed to the temporal discretization of off-lattice Boltzmann methods, which is independent of the discretization of space and velocity space.

Differences were also identified in terms of accuracy. The D3Q13 and D3Q21 based on icosahedra and dodecahedra, shown in Fig. 2, proved to be both efficient and accurate off-lattice velocity sets for weakly compressible flows. Both velocity sets showed a better enstrophy agreement with the reference solution in underresolved flow simulations. The reason for this is not necessarily that the precision of the cubature is higher since the degree of precision of the D3Q13, D3Q21, and D3Q27 velocity sets is identical. Instead, we attribute the better agreement of the enstrophy with the reference to the fewer advection equations that have to be solved connected with fewer interpolation steps, leading to less artificial diffusion. Moreover, due to their derivation from platonic solids, these velocity sets exhibit high geometric isotropy, which is favorable for the simulation of turbulent flows. These geometric considerations are probably also the reason why the D3Q21 outperforms the D3Q13 velocity set in terms of enstrophy. However, simulations with all of these degree-five velocity sets are affected by the cubic error term, being dependent on the Mach number. Obviously, this error term also spoils the simulations since the Mach number of Ma = 0.1 is not negligible. The degree-seven velocity set D3V27 with the aim to eliminate these cubic errors in the model proved to be more accurate than the on-lattice D3Q27, but coming at a comparable price. Despite the numerical diffusion introduced by the SLLBM, we showed in past works that the spatial convergence order corresponds to the order of the finite element [45]. By contrast, the spatial convergence order of on-lattice Boltzmann methods is restricted to second order.

Numerical diffusion and dispersion are critical issues of off-lattice Boltzmann methods compared to on-lattice Boltzmann methods, resulting from the interpolation in the case of the SLLBM. High-order interpolation polynomials as used in the present article, however, significantly lower the dissipative effects in the simulation [45]. Contrary to that, on-lattice Boltzmann methods are valued for low dissipation [76] due to the exact streaming step, but they suffer from instabilities at high Reynolds numbers when applying the usual BGK collision operator. To encounter these stability issues, several collision models have been proposed to stabilize simulations by introducing minimal diffusion without sacrificing the collision operator's locality. Examples are multi-relaxation time (MRT) [77–80], central MRT [81,82], entropic [83,84], regularized [85,86], or cumulant models [87,88]. Due to the non-negligible amount of dissipation evoked by the streaming step of off-lattice Boltzmann schemes, these established on-lattice collision models likely fulfil a different role in off-lattice LBM. Nevertheless, previous work has utilized the semi-Lagrangian streaming step in combination with a stabilized collision model [40]. Consequently, future research is necessary to clarify the impact of collision models on off-lattice Boltzmann methods.

Finally, some technical aspects need to be discussed. In particular, the streaming step's implementations of on-lattice and off-lattice Boltzmann methods are significantly different. On the one hand, the exact streaming step of on-lattice Boltzmann methods can naively be implemented by on-board routines of many software packages, e.g. by "numpy.roll" in Numpy [89]. On the other hand, the interpolation routines of the SLLBM require a thoughtful implementation, especially when following our recommendation to employ high-order polynomials with non-equidistant support points and cell-wise organization. For this task, a matured finite element library like deal.ii is helpful [54]. The execution time of the semi-Lagrangian streaming step is one magnitude larger [45] for the same configuration and velocity set. Despite the computational overhead, off-lattice Boltzmann methods have proven beneficial for unstructured meshes or compressible simulations [40,44,45]. More appropriate velocity sets, as presented in this article, further reduce the gap in computation cost, as the computational complexity of the SLLBM scales linearly with respect to the number of discrete velocities.

In summary, off-lattice Boltzmann methods relax the LBM in terms of the velocity space discretization. As sparse numerical cubatures are still progressing, the present work lays the foundations to directly utilize new cubature rules in CFD simulations with off-lattice Boltzmann methods.

6. Conclusion

This paper studied the utilization of cubature rules in off-lattice Boltzmann methods for weakly and fully compressible flows. The deduced off-lattice velocity sets presented in this article reduce the number of discrete velocities and increase the accuracy of the simulation.

Table C.9
Abscissae ξ_i and weights w_i for the D2Q19 velocity set.

i	w_i	ξ_{ix}	ξ_{iy}
0	0.3168437267921905	0.0	0.0
1,2	0.10558878375062891	±1.4869982213169028	0.0
3, 4, 5, 6	0.10242471232109360	±0.775196278121181	±1.367469636752619
7, 8, 9, 10	0.00953510698543825	±2.5175897644357486	±1.105629214668943
11,12	0.006865104210104631	0.0	±2.9213306655318734
13, 14, 15, 16	0.002405335328939458	±1.8663975507141328	±2.6987507639352253
17,18	0.0003939393722285871	±3.8358342053914734	0.0

$c_s = 1$.

In addition, fully compressible off-lattice simulations with degree-nine velocity sets feature better stability than the corresponding on-lattice counterparts. Taken together, cubature rule-derived off-lattice velocity sets are a viable alternative to the customary on-lattice Boltzmann velocity sets and should have priority in off-lattice Boltzmann simulations.

CRediT authorship contribution statement

Dominik Wilde: Conceptualization, Methodology, Software, Validation, Writing - original draft. **Andreas Krämer:** Software, Writing - review & editing. **Mario Bedrunka:** Software, Writing - review & editing. **Dirk Reith:** Supervision, Writing - review & editing, Resources. **Holger Foysi:** Supervision, Writing - review & editing, Funding acquisition.

Declaration of competing interest

The authors declare that they have no known competing financial interests or personal relationships that could have appeared to influence the work reported in this paper.

Acknowledgments

We gratefully acknowledge support for D.W. by German Research Foundation (DFG) project FO 674/17-1. The simulations were performed using the Platform for Scientific Computing at Bonn-Rhein-Sieg University, which is funded by the German Ministry of Education and Research and the Ministry for Culture and Science North Rhine-Westfalia, Germany (research grant 13FH156IN6).

Appendix A. Hermite polynomials and moments

The scaled Hermite polynomials with $\hat{\xi}_i = \xi_i/c_s$ up to fourth order read

$$\mathcal{H}_i^{(0)} = 1$$
$$\mathcal{H}_{i\alpha}^{(1)} = \frac{\hat{\xi}_{i\alpha}}{c_s}$$
$$\mathcal{H}_{i\alpha\beta}^{(2)} = \frac{\hat{\xi}_{i\alpha}\hat{\xi}_{i\beta} - \delta_{\alpha\beta}}{c_s^2}$$
$$\mathcal{H}_{i\alpha\beta\gamma}^{(3)} = \frac{\hat{\xi}_{i\alpha}\hat{\xi}_{i\beta}\hat{\xi}_{i\gamma} - (\hat{\xi}_{i\alpha}\delta_{\beta\gamma} + \hat{\xi}_{i\beta}\delta_{\alpha\gamma} + \hat{\xi}_{i\gamma}\delta_{\alpha\beta})}{c_s^3}$$
$$\mathcal{H}_{i\alpha\beta\gamma\delta}^{(4)} = \frac{\hat{\xi}_{i\alpha}\hat{\xi}_{i\beta}\hat{\xi}_{i\gamma}\hat{\xi}_{i\delta} - \mathcal{T}_i + (\delta_{\alpha\beta}\delta_{\gamma\delta} + \delta_{\alpha\gamma}\delta_{\beta\delta} + \delta_{\alpha\delta}\delta_{\beta\gamma})}{c_s^4},$$

with

$$\mathcal{T}_i = \hat{\xi}_{i\alpha}\hat{\xi}_{i\beta}\delta_{\gamma\delta} + \hat{\xi}_{i\alpha}\hat{\xi}_{i\gamma}\delta_{\beta\delta} + \hat{\xi}_{i\alpha}\hat{\xi}_{i\delta}\delta_{\beta\gamma} + \hat{\xi}_{i\beta}\hat{\xi}_{i\gamma}\delta_{\alpha\delta} + \hat{\xi}_{i\beta}\hat{\xi}_{i\delta}\delta_{\alpha\gamma} + \hat{\xi}_{i\gamma}\hat{\xi}_{i\delta}\delta_{\alpha\beta}.$$

The moments of the Boltzmann equation up to fourth order are

$$\begin{aligned}
a_{eq}^{(0)} &= \rho \\
a_{\alpha,eq}^{(1)} &= \rho u_\alpha \\
a_{\alpha\beta,eq}^{(2)} &= \rho(u_\alpha u_\beta + T_0(\theta-1)\delta_{\alpha\beta}) \\
a_{\alpha\beta\gamma,eq}^{(3)} &= \rho\left[u_\alpha u_\beta u_\gamma + T_0(\theta-1)(\delta_{\alpha\beta}u_\gamma + \delta_{\alpha\gamma}u_\beta + \delta_{\beta\gamma}u_\alpha)\right] \\
a_{\alpha\beta\gamma\delta,eq}^{(4)} &= \rho[u_\alpha u_\beta u_\gamma u_\delta + T_0(\theta-1)((\delta_{\alpha\beta}\delta_{\gamma\delta} + \delta_{\alpha\gamma}\delta_{\beta\delta} + \delta_{\alpha\delta}\delta_{\beta\gamma})T_0(\theta-1) \\
&\quad + \delta_{\alpha\beta}u_\gamma u_\delta + \delta_{\alpha\gamma}u_\beta u_\delta + \delta_{\alpha\delta}u_\beta u_\gamma + \\
&\quad \delta_{\beta\gamma}u_\alpha u_\delta + \delta_{\beta\delta}u_\alpha u_\gamma + \delta_{\gamma\delta}u_\alpha u_\beta)].
\end{aligned}$$

Appendix B. Symmetry conditions

The symmetry conditions from zeroth to ninth order are

$$\sum_i w_i = 1$$
$$\sum_i w_i\xi_{i\alpha} = 0$$
$$\sum_i w_i\xi_{i\alpha}\xi_{i\beta} = c_s^2\delta_{\alpha\beta}$$
$$\sum_i w_i\xi_{i\alpha}\xi_{i\beta}\xi_{i\gamma} = 0$$
$$\sum_i w_i\xi_{i\alpha}\xi_{i\beta}\xi_{i\gamma}\xi_{i\delta} = c_s^4\Delta_{\alpha\beta\gamma\delta}$$
$$\sum_i w_i\xi_{i\alpha}\xi_{i\beta}\xi_{i\gamma}\xi_{i\delta}\xi_{i\epsilon} = 0$$
$$\sum_i w_i\xi_{i\alpha}\xi_{i\beta}\xi_{i\gamma}\xi_{i\delta}\xi_{i\epsilon}\xi_{i\zeta} = c_s^6\Delta_{\alpha\beta\gamma\delta\epsilon\zeta}$$
$$\sum_i w_i\xi_{i\alpha}\xi_{i\beta}\xi_{i\gamma}\xi_{i\delta}\xi_{i\epsilon}\xi_{i\zeta}\xi_{i\eta} = 0$$
$$\sum_i w_i\xi_{i\alpha}\xi_{i\beta}\xi_{i\gamma}\xi_{i\delta}\xi_{i\epsilon}\xi_{i\zeta}\xi_{i\eta}\xi_{i\theta} = c_s^8\Delta_{\alpha\beta\gamma\delta\epsilon\zeta\eta\theta}$$
$$\sum_i w_i\xi_{i\alpha}\xi_{i\beta}\xi_{i\gamma}\xi_{i\delta}\xi_{i\epsilon}\xi_{i\zeta}\xi_{i\eta}\xi_{i\theta}\xi_{il} = 0,$$

with

$$\Delta_{\alpha\beta\gamma\delta} = \delta_{\alpha\beta}\delta_{\gamma\delta} + \delta_{\alpha\gamma}\delta_{\beta\delta} + \delta_{\alpha\delta}\delta_{\beta\gamma},$$

as well as

$$\Delta_{\alpha\beta\gamma\delta\epsilon\zeta} = \delta_{\alpha\beta}\Delta_{\gamma\delta\epsilon\zeta} + \delta_{\alpha\gamma}\Delta_{\beta\delta\epsilon\zeta} + \delta_{\alpha\delta}\Delta_{\beta\gamma\epsilon\zeta} + \delta_{\alpha\epsilon}\Delta_{\beta\gamma\delta\zeta} + \delta_{\alpha\zeta}\Delta_{\beta\gamma\delta\epsilon},$$

and

$$\Delta_{\alpha\beta\gamma\delta\epsilon\zeta\eta\theta} = \delta_{\alpha\beta}\Delta_{\gamma\delta\epsilon\zeta\eta\theta} + \delta_{\alpha\gamma}\Delta_{\beta\delta\epsilon\zeta\eta\theta} + \delta_{\alpha\delta}\Delta_{\beta\gamma\epsilon\zeta\eta\theta} + \delta_{\alpha\epsilon}\Delta_{\beta\gamma\delta\zeta\eta\theta} + \delta_{\alpha\zeta}\Delta_{\beta\gamma\delta\epsilon\eta\theta} + \delta_{\alpha\eta}\Delta_{\beta\gamma\delta\epsilon\zeta\theta} + \delta_{\alpha\theta}\Delta_{\beta\gamma\delta\epsilon\zeta\eta}.$$

Appendix C. D2Q19 velocity set

See Table C.9.

Appendix D. D3V27 velocity set

See Table D.10.

Table D.10
Abscissae ξ_i and weights w_i for the D2V27 velocity set.

i	w_i	ξ_{ix}	ξ_{iy}	ξ_{iz}	
0	0.31247897198654906	0.0	0.0	0.0	
1, … , 8	0.06338446047675325	±1.1198362860638005	±1.1198362860638005	±1.1198362860638005	
9, … , 14	0.029035130153906134	±2.358709038202103	0.0	0.0	(cyc)
15, … , 26	0.0005195469396656799	±3.142130383387586	±3.142130383387586	0.0	(cyc)

$c_s = 1$.

Table E.11
Abscissae ξ_i and weights w_i for the D3Q45 velocity set.

w_i	ξ_{ix}	ξ_{iy}	ξ_{iz}
0.20740740740740618	0.0	0.0	0.0
0.05787037037037047	0.06386083877343968	−1.2239121278243665	−1.2239121278243665
0.05787037037037047	−0.06386083877343968	1.2239121278243665	1.2239121278243665
0.05787037037037047	1.2239121278243665	−0.06386083877343968	1.2239121278243665
0.05787037037037047	−1.2239121278243665	0.06386083877343968	−1.2239121278243665
0.05787037037037047	1.2239121278243665	1.2239121278243665	−0.06386083877343968
0.05787037037037047	−1.2239121278243665	−1.2239121278243665	0.06386083877343968
0.05787037037037047	1.5766994272507744	−0.5069610024977665	−0.5069610024977665
0.05787037037037047	−1.5766994272507744	0.5069610024977665	0.5069610024977665
0.05787037037037047	0.5069610024977665	0.5069610024977665	−1.5766994272507744
0.05787037037037047	−0.5069610024977665	−0.5069610024977665	1.5766994272507744
0.05787037037037047	−0.5069610024977665	1.5766994272507744	−0.5069610024977665
0.05787037037037047	0.5069610024977665	−1.5766994272507744	0.5069610024977665
0.00462962962962958	2.403092127540177	0.8892242114059369	−1.5602655313772367
0.00462962962962958	−2.403092127540177	−0.8892242114059369	1.5602655313772367
0.00462962962962958	−2.403092127540177	1.5602655313772367	−0.8892242114059369
0.00462962962962958	2.403092127540177	−1.5602655313772367	0.8892242114059369
0.00462962962962958	−0.8892242114059369	−2.403092127540177	1.5602655313772367
0.00462962962962958	0.8892242114059369	2.403092127540177	−1.5602655313772367
0.00462962962962958	−0.8892242114059369	1.5602655313772367	−2.403092127540177
0.00462962962962958	0.8892242114059369	−1.5602655313772367	2.403092127540177
0.00462962962962958	−1.5602655313772367	0.8892242114059369	2.403092127540177
0.00462962962962958	−1.5602655313772367	2.403092127540177	0.8892242114059369
0.00462962962962958	1.5602655313772367	−0.8892242114059369	−2.403092127540177
0.00462962962962958	1.5602655313772367	−2.403092127540177	−0.8892242114059369
0.00462962962962958	0.4744978678080795	0.4744978678080795	2.9239876105912574
0.00462962962962958	0.4744978678080795	2.9239876105912574	0.4744978678080795
0.00462962962962958	−0.4744978678080795	−0.4744978678080795	−2.9239876105912574
0.00462962962962958	−0.4744978678080795	−2.9239876105912574	−0.4744978678080795
0.00462962962962958	2.9239876105912574	0.4744978678080795	0.4744978678080795
0.00462962962962958	−2.9239876105912574	−0.4744978678080795	−0.4744978678080795
0.00462962962962958	1.7320508075688787	1.7320508075688787	1.7320508075688787
0.00462962962962958	−1.7320508075688787	−1.7320508075688787	−1.7320508075688787
0.0004629629629629939	−2.7367507163016924	0.14279717659756475	−2.7367507163016924
0.0004629629629629939	2.7367507163016924	2.7367507163016924	−0.14279717659756475
0.0004629629629629939	2.7367507163016924	−0.14279717659756475	2.7367507163016924
0.0004629629629629939	−2.7367507163016924	−2.7367507163016924	0.14279717659756475
0.0004629629629629939	0.14279717659756475	−2.7367507163016924	−2.7367507163016924
0.0004629629629629939	−0.14279717659756475	2.7367507163016924	2.7367507163016924
0.0004629629629629939	−3.5256070994177073	1.1335992635264445	1.1335992635264445
0.0004629629629629939	3.5256070994177073	−1.1335992635264445	−1.1335992635264445
0.0004629629629629939	1.1335992635264445	−3.5256070994177073	1.1335992635264445
0.0004629629629629939	−1.1335992635264445	3.5256070994177073	−1.1335992635264445
0.0004629629629629939	1.1335992635264445	1.1335992635264445	−3.5256070994177073
0.0004629629629629939	−1.1335992635264445	−1.1335992635264445	3.5256070994177073

$c_s = 1$.

Appendix E. D3Q45 velocity set

See Table E.11.

References

[1] Guy R. McNamara, Gianluigi Zanetti, Use of the boltzmann equation to simulate lattice-gas automata, Phys. Rev. Lett. (1988).

[2] F.J. Higuera, J. Jiménez, Boltzmann approach to lattice gas simulations, Europhys. Lett. (1989).

[3] Shiyi Chen, Hudong Chen, Daniel Martnez, William Matthaeus, Lattice Boltzmann model for simulation of magnetohydrodynamics, Phys. Rev. Lett. (1991).

[4] Timm Krüger, Halim Kusumaatmaja, Alexander Kuzmin, Orest Shardt, Goncalo Silva, Erlend Magnus Viggen, The Lattice Boltzmann Method: Principles and Practice, Springer, 2017.

[5] Pierre Lallemand, Li-shi Luo, Manfred Krafczyk, Wen-an Yong, The lattice Boltzmann method for nearly incompressible flows, J. Comput. Phys. (2020) 109713.

[6] Tadeusz Platkowski, Reinhard Illner, Discrete velocity models of the Boltzmann equation: A survey on the mathematical aspects of the theory, SIAM Rev. 30 (2) (1988) 213–255.

[7] Li Shi Luo, Some recent results on discrete velocity models and ramifications for lattice Boltzmann equation, Comput. Phys. Comm. 129 (1) (2000) 63–74.

[8] Mingde Su, Kun Xu, M.S. Ghidaoui, Low-speed flow simulation by the gas-kinetic scheme, J. Comput. Phys. (1999).

[9] Kun Xu, Juan Chen Huang, A unified gas-kinetic scheme for continuum and rarefied flows, J. Comput. Phys. 229 (20) (2010) 7747–7764.

[10] Xiaoyi He, Xiaowen Shan, Gary D. Doolen, Discrete Boltzmann equation model for nonideal gases, Phys. Rev. E 57 (1) (1998) R13–R16.

[11] Christophe Coreixas, Gauthier Wissocq, Guillaume Puigt, Jean François Boussuge, Pierre Sagaut, Recursive regularization step for high-order lattice Boltzmann methods, Phys. Rev. E 96 (3) (2017).

[12] Xiaowen Shan, Xiaoyi He, Discretization of the velocity space in the solution of the Boltzmann equation, Phys. Rev. Lett. 80 (1) (1998) 65–68.

[13] Xiaowen Shan, Xue Feng Yuan, Hudong Chen, Kinetic theory representation of hydrodynamics: A way beyond the Navier-Stokes equation, J. Fluid Mech. 550 (-1) (2006) 413–441.

[14] Ienkaran Arasaratnam, Simon Haykin, Cubature kalman filters, IEEE Trans. Automat. Control 54 (6) (2009) 1254–1269.

[15] A.H. Stroud, Approximate calculation of multiple integrals, Math. Comp. (1973).

[16] Ronald Cools, Philip Rabinowitz, Monomial cubature rules since "stroud": a compilation, J. Comput. Appl. Math. 48 (3) (1993) 309–326.

[17] Ronald Cools, An encyclopaedia of cubature formulas, J. Complexity 19 (3) (2003) 445–453, Oberwolfach Special Issue.

[18] Xiaoyi He, Li Shi Luo, Theory of the lattice Boltzmann method: From the Boltzmann equation to the lattice Boltzmann equation, Phys. Rev. E 55 (6) (1997) 6811–6820.

[19] Alexander Thomas White, Chuh Khiun Chong, Rotational invariance in the three-dimensional lattice Boltzmann method is dependent on the choice of lattice, J. Comput. Phys. 230 (16) (2011) 6367–6378.

[20] Goncalo Silva, Viriato Semiao, Truncation errors and the rotational invariance of three-dimensional lattice models in the lattice Boltzmann method, J. Comput. Phys. (2014).

[21] Martin Bauer, Goncalo Silva, Ulrich Rüde, Truncation errors of the d3q19 lattice model for the lattice boltzmann method, J. Comput. Phys. 405 (2020) 109111.

[22] Manjusha Namburi, Siddharth Krithivasan, Santosh Ansumali, Crystallographic lattice boltzmann method, Sci. Rep. 6 (2016).

[23] Y.H. Qian, S.A. Orszag, Lattice BGK models for the Navier-Stokes equation: Nonlinear deviation in compressible regimes, Europhys. Lett. (EPL) 21 (3) (1993) 255–259.

[24] Paulo C. Philippi, Luiz A. Hegele, Luís O.E. Dos Santos, Rodrigo Surmas, From the continuous to the lattice Boltzmann equation: The discretization problem and thermal models, Phys. Rev. E 73 (5) (2006).

[25] Xiaowen Shan, The mathematical structure of the lattices of the lattice Boltzmann method, J. Comput. Sci. 17 (2016) 475–481.

[26] N. Frapolli, S.S. Chikatamarla, I.V. Karlin, Entropic lattice Boltzmann model for compressible flows, Phys. Rev. E 92 (6) (2015) 061301.

[27] Jianping Meng, Yonghao Zhang, Accuracy analysis of high-order lattice Boltzmann models for rarefied gas flows, J. Comput. Phys. 230 (3) (2011) 835–849.

[28] Shyam S. Chikatamarla, Iliya V. Karlin, Lattices for the lattice Boltzmann method, Phys. Rev. E 79 (4) (2009).

[29] Xiaowen Shan, General solution of lattices for cartesian lattice bhatanagar-gross-krook models, Phys. Rev. E 81 (3) (2010) 1–7.

[30] R. Surmas, Capico E. Pico Ortiz, P.C. Philippi, Simulating thermohydrodynamics by finite difference solutions of the Boltzmann equation, Eur. Phys. J.: Spec. Top. 171 (1) (2009) 81–90.

[31] Wahyu Perdana Yudistiawan, Sang Kyu Kwak, D.V. Patil, Santosh Ansumali, Higher-order galilean-invariant lattice Boltzmann model for microflows: Single-component gas, Phys. Rev. E 82 (4) (2010).

[32] Akinori Tamura, Keita Okuyama, Shiro Takahashi, Masaya Ohtsuka, Three-dimensional discrete-velocity BGK model for the incompressible Navier-Stokes equations, Comput. Fluids 40 (1) (2011) 149–155.

[33] Andreas Krämer, Knut Küllmer, Dirk Reith, Wolfgang Joppich, Holger Foysi, Semi-Lagrangian off-lattice Boltzmann method for weakly compressible flows, Phys. Rev. E 95 (2) (2017).

[34] Nianzheng Cao, Shiyi Chen, Shi Jin, Daniel Martínez, Physical symmetry and lattice symmetry in the lattice Boltzmann method, Phys. Rev. E 55 (1) (1997) R21–R24.

[35] Kazem Hejranfar, Mohammad Hossein Saadat, Sina Taheri, High-order weighted essentially nonoscillatory finite-difference formulation of the lattice Boltzmann method in generalized curvilinear coordinates, Phys. Rev. E 95 (2) (2017) 23314.

[36] Francesca Nannelli, Sauro Succi, The lattice Boltzmann equation on irregular lattices, J. Stat. Phys. 68 (3–4) (1992) 401–407.

[37] Weidong Li, Li-Shi Luo, An implicit block lu-sgs finite-volume lattice-boltzmann scheme for steady flows on arbitrary unstructured meshes, J. Comput. Phys. 327 (2016) 503–518.

[38] Xing Shi, Jianzhong Lin, Zhaosheng Yu, Discontinuous Galerkin spectral element lattice Boltzmann method on triangular element, Internat. J. Numer. Methods Fluids 42 (11) (2003) 1249–1261.

[39] Misun Min, Taehun Lee, A spectral-element discontinuous Galerkin lattice Boltzmann method for nearly incompressible flows, J. Comput. Phys. 230 (1) (2011) 245–259.

[40] G Di Ilio, B Dorschner, G Bella, S Succi, I V Karlin, Simulation of turbulent flows with the entropic multirelaxation time lattice Boltzmann method on body-fitted meshes, J. Fluid Mech. 849 (2018) 35–56.

[41] B. Dorschner, F. Bösch, I.V. Karlin, Particles on demand for kinetic theory, Phys. Rev. Lett. 121 (13) (2018).

[42] Mohammad Hossein Saadat, Fabian Bösch, Ilya V. Karlin, Lattice Boltzmann model for compressible flows on standard lattices: Variable prandtl number and adiabatic exponent, Phys. Rev. E 99 (1) (2019) 013306.

[43] E. Reyhanian, B. Dorschner, I.V. Karlin, Thermokinetic lattice Boltzmann model of nonideal fluids, Phys. Rev. E 102 (2) (2020) 1–5.

[44] Dominik Wilde, Andreas Krämer, Dirk Reith, Holger Foysi, Semi-Lagrangian lattice Boltzmann method for compressible flows, Phys. Rev. E 101 (2020) 053306.

[45] Andreas Krämer, Dominik Wilde, Knut Küllmer, Dirk Reith, Holger Foysi, Wolfgang Joppich, Lattice Boltzmann simulations on irregular grids: Introduction of the natrium library, Comput. Math. Appl. 79 (1) (2020) 34–54.

[46] M.H. Saadat, F. Bösch, I.V. Karlin, Semi-Lagrangian lattice Boltzmann model for compressible flows on unstructured meshes, Phys. Rev. E 101 (2) (2020) 23311.

[47] Xiaobo Nie, Xiaowen Shan, Hudong Chen, Thermal lattice Boltzmann model for gases with internal degrees of freedom, Phys. Rev. E 77 (3) (2008) 1–4.

[48] Ann Haegemans, Robert Piessens, Construction of Cubature formulas of degree seven and nine symmetric planar regions, using orthogonal polynomials, SIAM J. Numer. Anal. 14 (3) (1977) 492–508.

[49] A.H. Stroud, Some seventh degree integration formulas for symmetric regions, SIAM J. Numer. Anal. 4 (1) (1967) 37–44.

[50] SI Konyaev, Ninth-order quadrature formulas invariant with respect to the icosahedral group, in: Doklady Akademii Nauk, Vol. 233, Russian Academy of Sciences, 1977, pp. 784–787.

[51] James R. Van Zandt, Efficient cubature rules, ETNA - Electron. Trans. Numer. Anal. 51 (2019) 219–239.

[52] Dominik Wilde, Andreas Krämer, Dirk Reith, Holger Foysi, High-order semi-Lagrangian kinetic scheme for compressible turbulence, Phys. Rev. E (2020) submitted for publication.

[53] U. Frisch, B. Hasslacher, Y. Pomeau, Lattice-gas automata for the Navier-Stokes equation, Phys. Rev. Lett. 56 (14) (1986) 1505–1508.

[54] Daniel Arndt, Wolfgang Bangerth, Bruno Blais, Thomas C. Clevenger, Marc Fehling, Alexander V. Grayver, Timo Heister, Luca Heltai, Martin Kronbichler, Matthias Maier, Peter Munch, Jean-Paul Pelteret, Reza Rastak, Ignacio Thomas, Bruno Turcksin, Zhuoran Wang, David Wells, The deal.ii library, version 9.2, J. Numer. Math. 28 (3) (2020) 131–146.

[55] Andreas Krämer, Dominik Wilde, Mario Bedrunka, Lettuce: PyTorch-based Lattice Boltzmann Solver, 2020.

[56] Mario Bedrunka, Dominik Wilde, Martin Kliemank, Dirk Reith, Holger Foysi, Andreas Krämer, Lettuce: PyTorch-based Lattice Boltzmann framework.

[57] Adam Paszke, Sam Gross, Francisco Massa, Adam Lerer, James Bradbury, Gregory Chanan, Trevor Killeen, Zeming Lin, Natalia Gimelshein, Luca Antiga, Alban Desmaison, Andreas Kopf, Edward Yang, Zachary DeVito, Martin Raison, Alykhan Tejani, Sasank Chilamkurthy, Benoit Steiner, Lu Fang, Junjie Bai, Soumith Chintala, Pytorch: An imperative style, high-performance deep learning library, in: H. Wallach, H. Larochelle, A. Beygelzimer, F. d' Alché-Buc, E. Fox, R. Garnett (Eds.), Advances in Neural Information Processing Systems, Vol. 32, Curran Associates, Inc., 2019, pp. 8024–8035.

[58] Marc E. Brachet, Daniel I. Meiron, Steven A. Orszag, B.G. Nickel, Rudolf H. Morf, Uriel Frisch, Small-scale structure of the taylor–green vortex, J. Fluid Mech. 130 (-1) (1983) 411.

[59] Osamu Inoue, Yuji Hattori, Sound generation by shock-vortex interactions, J. Fluid Mech. 380 (1999) 81–116.

[60] Andreas Krämer, Dominik Wilde, Knut Küllmer, Dirk Reith, Holger Foysi, Pseudoentropic derivation of the regularized lattice Boltzmann method, Phys. Rev. E 100 (2) (2019) 023302.

[61] Nikolaus A. Adams, Stefan Hickel, Implicit large-eddy simulation: Theory and application, in: Advances in Turbulence, Vol. XII, Springer Berlin Heidelberg, Berlin, Heidelberg, 2009, pp. 743–750.

[62] Naifu Peng, Yue Yang, Effects of the mach number on the evolution of vortex-surface fields in compressible taylor-green flows, Phys. Rev. Fluids 3 (1) (2018) 1–21.

[63] Christophe Coreixas, High-Order Extension of the Recursive Regularized Lattice Boltzmann Method (Ph.D. thesis), INP Toulouse, 2018.

[64] Dominic Spiller, Burkhard Dünweg, Semiautomatic construction of lattice Boltzmann models, Phys. Rev. E 101 (2020) 043310.

[65] Yongliang Feng, Pierre Sagaut, Wen Quan Tao, A compressible lattice Boltzmann finite volume model for high subsonic and transonic flows on regular lattices, Comput. Fluids 131 (2016) 45–55.

[66] Yongliang Feng, Pierre Boivin, Jérôme Jacob, Pierre Sagaut, Hybrid recursive regularized thermal lattice Boltzmann model for high subsonic compressible flows, J. Comput. Phys. 394 (2019) 82–99.

[67] Florian Renard, Yongliang Feng, Jean François Boussuge, Pierre Sagaut, Improved compressible hybrid lattice Boltzmann method on standard lattice for subsonic and supersonic flows, Comput. Fluids 219 (2021) 104867.

[68] Florian Renard, G. Wissocq, Jean franccois Boussuge, P. Sagaut, A linear stability analysis of compressible hybrid lattice Boltzmann methods, arXiv: Comput. Phys. (2020).

[69] Nicolò Frapolli, S.S. Chikatamarla, I.V. Karlin, Entropic lattice Boltzmann model for gas dynamics: Theory, boundary conditions, and implementation, Phys. Rev. E 93 (6) (2016) 063302.
[70] Mohammad Atif, Manjusha Namburi, Santosh Ansumali, Higher-order lattice Boltzmann model for thermohydrodynamics, Phys. Rev. E 98 (5) (2018) 053311.
[71] Jonas Latt, Christophe Coreixas, Joël Beny, Andrea Parmigiani, Efficient supersonic flow simulations using lattice Boltzmann methods based on numerical equilibria, Phil. Trans. R. Soc. A 378 (2175) (2020) 20190559.
[72] Nicolò Frapolli, S.S. Chikatamarla, I.V. Karlin, Lattice kinetic theory in a comoving galilean reference frame, Phys. Rev. Lett. 117 (1) (2016) 10604.
[73] S.A. Hosseini, C. Coreixas, N. Darabiha, D. Thévenin, Extensive analysis of the lattice Boltzmann method on shifted stencils, Phys. Rev. E 100 (6) (2019) 1–15.
[74] Christophe Coreixas, Jonas Latt, Compressible lattice Boltzmann methods with adaptive velocity stencils: An interpolation-free formulation, Phys. Fluids (2020).
[75] Zhaoli Guo, Jianchun Wang, Simulation of three-dimensional compressible turbulence using the discrete unified gas kinetic scheme, Phys. Fluids 125104 (2020).
[76] Simon Marié, Denis Ricot, Pierre Sagaut, Comparison between lattice Boltzmann method and Navier-Stokes high order schemes for computational aeroacoustics, J. Comput. Phys. 228 (4) (2009) 1056–1070.
[77] Y.H. Qian, D D'Humières, P. Lallemand, Lattice BGK models for Navier-Stokes equation, Europhys. Lett. 17 (6) (1992) 479–484.
[78] Dominique D'Humières, Irina Ginzburg, Manfred Krafczyk, Pierre Lallemand, Li Shi Luo, Multiple-relaxation-time lattice Boltzmann models in three dimensions, Philos. Trans. R. Soc. A 360 (1792) (2002) 437–451.
[79] Paul J. Dellar, Incompressible limits of lattice Boltzmann equations using multiple relaxation times, J. Comput. Phys. 190 (2) (2003) 351–370.
[80] Xiaowen Shan, Hudong Chen, A general multiple-relaxation-time Boltzmann collision model, Internat. J. Modern Phys. C 18 (04) (2007) 635–643.
[81] Martin Geier, Andreas Greiner, Jan G. Korvink, Cascaded digital lattice Boltzmann automata for high Reynolds number flow, Phys. Rev. E 73 (6) (2006) 1–10.
[82] Xiaowen Shan, Central-moment-based galilean-invariant multiple-relaxation-time collision model, Phys. Rev. E 100 (2019) 043308.
[83] I.V. Karlin, A. Ferrante, H.C. Öttinger, Perfect entropy functions of the lattice Boltzmann method, Europhys. Lett. 47 (2) (1999) 182–188.
[84] Mohammad Atif, Praveen Kumar Kolluru, Chakradhar Thantanapally, Santosh Ansumali, Essentially entropic lattice Boltzmann model, Phys. Rev. Lett. 119 (24) (2017) 1–5.
[85] Jonas Latt, Bastien Chopard, Lattice Boltzmann method with regularized pre-collision distribution functions, Math. Comput. Simulation 72 (2–6) (2006) 165–168.
[86] Orestis Malaspinas, Increasing stability and accuracy of the lattice Boltzmann scheme: recursivity and regularization, 2015, pp. 1–31.
[87] Martin Geier, Martin Schönherr, Andrea Pasquali, Manfred Krafczyk, The cumulant lattice Boltzmann equation in three dimensions: Theory and validation, Comput. Math. Appl. 70 (4) (2015) 507–547.
[88] Martin Geier, Stephan Lenz, Martin Schönherr, Manfred Krafczyk, Under-resolved and large eddy simulations of a decaying taylor–green vortex with the cumulant lattice Boltzmann method, Theor. Comput. Fluid Dyn. (2020).
[89] Charles R. Harris, K. Jarrod Millman, St'efan J. van der Walt, Ralf Gommers, Pauli Virtanen, David Cournapeau, Eric Wieser, Julian Taylor, Sebastian Berg, Nathaniel J. Smith, Robert Kern, Matti Picus, Stephan Hoyer, Marten H. van Kerkwijk, Matthew Brett, Allan Haldane, Jaime Fern'andez del R'ıo, Mark Wiebe, Pearu Peterson, Pierre G'erard-Marchant, Kevin Sheppard, Tyler Reddy, Warren Weckesser, Hameer Abbasi, Christoph Gohlke, Travis E. Oliphant, Array programming with numpy, Nature 585 (7825) (2020) 357–362.

Dominik Wilde is a research assistant at the University of Siegen, Germany and Bonn-Rhein-Sieg University of Applied Sciences. He holds an M. Sc. degree in aerospace engineering from the Bundeswehr University Munich and currently pursues a Ph.D. on semi-Lagrangian off-lattice Boltzmann methods.

Andreas Krämer is at the Artificial Intelligence for the Sciences group at Freie Universität (FU) Berlin. He studied mathematics at the University of Trier and holds a Ph.D. from the University of Siegen, Germany. After completing his Ph.D. on off-lattice Boltzmann methods in 2017 he worked for two years as a postdoc at the National Institutes of Health (NIH), United States. His research interests are machine learning, molecular dynamics, and lattice Boltzmann methods.

Mario Bedrunka is research assistant at the University of Siegen, Germany and Bonn-Rhein-Sieg University of Applied Sciences. He holds an M. Eng. degree in mechanical engineering from the Bonn-Rhein-Sieg University of Applied Sciences. Now he pursues a Ph.D. on machine learning in the lattice Boltzmann methods and the modeling and simulation of hydrogen storages.

Dirk Reith studied physics and mathematics at Mainz (Germany) and Uppsala (Sweden) University. After receiving his diploma in 1998, he was a guest researcher at the Australian National University, Canberra. In 1999, he joined the MPI for Polymer Research, Mainz, where he completed his Ph.D. in physical chemistry in 2001. From 2002–2006, Dirk Reith worked as an IT-Project Manager at DaimlerChrysler, Stuttgart. Thereafter, he founded the Computational Chemical Engineering Group at the Fraunhofer Institute SCAI, Sankt Augustin. Since 2012, he holds a professorship for modeling and simulation engineering at BRSU with research emphasis in soft matter, materials, and simulation methods.

Holger Foysi is head of the chair of fluid mechanics at the University of Siegen. He studied physics at the Technische Universität München (TUM) before joining the chair of fluid mechanics at TUM for his Ph.D. on turbulent supersonic channel flow and scalar transport. Following that, he pursued a postdoc at the department of mechanical engineering at UCSD San Diego, funded by a Feodor-Lynen fellowship. Before being appointed professor at Siegen, he received an Emmy-Noether fellowship to build a research group on turbulence control at the Institute of Fluid Mechanics and Aerodynamic Institute, RWTH Aachen.